Research Article | Vol. 24, No. 19 | 19 Sep 2016 | OPTICS EXPRESS 21474

Optics EXPRESS

Adaptive multiphoton endomicroscopy through a dynamically deformed multicore optical fiber using proximal detection

SEAN C. WARREN,[1,4] YOUNGCHAN KIM,[1,4] JAMES M. STONE,[2] CLAIRE MITCHELL,[1] JONATHAN C. KNIGHT,[2] MARK A. A. NEIL,[1] CARL PATERSON,[1] PAUL M. W. FRENCH,[1,4] AND CHRIS DUNSBY[1,3,4,*]

[1]*Photonics Group, Department of Physics, Imperial College London, London, SW7 2AZ, UK*
[2]*Department of Physics, University of Bath, Bath, BA2 7AY, UK*
[3]*Centre for Pathology, Imperial College London, London, W12 0NN, UK*
[4]*Authors contributed equally to this work*
[*]*christopher.dunsby@imperial.ac.uk*

Abstract: This paper demonstrates multiphoton excited fluorescence imaging through a polarisation maintaining multicore fiber (PM-MCF) while the fiber is dynamically deformed using all-proximal detection. Single-shot proximal measurement of the relative optical path lengths of all the cores of the PM-MCF in double pass is achieved using a Mach-Zehnder interferometer read out by a scientific CMOS camera operating at 416 Hz. A non-linear least squares fitting procedure is then employed to determine the deformation-induced lateral shift of the excitation spot at the distal tip of the PM-MCF. An experimental validation of this approach is presented that compares the proximally measured deformation-induced lateral shift in focal spot position to an independent distally measured ground truth. The proximal measurement of deformation-induced shift in focal spot position is applied to correct for deformation-induced shifts in focal spot position during raster-scanning multiphoton excited fluorescence imaging.

OCIS codes: (170.2150) Endoscopic imaging; (180.4315) Nonlinear microscopy; (180.5810) Scanning microscopy.

References and links

1. A. Volyar, A. Gnatovskii, N. Kukhtarev, and S. Lapaeva, "Image transmission via a multimode fiber assisted by polarization preserving phase conjugation in the photorefractive crystal," Appl. Phys. B **52**(6), 400–401 (1991).
2. S. Bianchi and R. Di Leonardo, "A multi-mode fiber probe for holographic micromanipulation and microscopy," Lab Chip **12**(3), 635–639 (2012).
3. T. Čižmár and K. Dholakia, "Exploiting multimode waveguides for pure fibre-based imaging," Nat. Commun. **3**, 1027 (2012).
4. Y. Choi, C. Yoon, M. Kim, T. D. Yang, C. Fang-Yen, R. R. Dasari, K. J. Lee, and W. Choi, "Scanner-free and wide-field endoscopic imaging by using a single multimode optical fiber," Phys. Rev. Lett. **109**(20), 203901 (2012).
5. I. N. Papadopoulos, S. Farahi, C. Moser, and D. Psaltis, "High-resolution, lensless endoscope based on digital scanning through a multimode optical fiber," Biomed. Opt. Express **4**(2), 260–270 (2013).
6. E. E. Morales-Delgado, S. Farahi, I. N. Papadopoulos, D. Psaltis, and C. Moser, "Delivery of focused short pulses through a multimode fiber," Opt. Express **23**(7), 9109–9120 (2015).
7. A. J. Thompson, C. Paterson, M. A. A. Neil, C. Dunsby, and P. M. W. French, "Adaptive phase compensation for ultracompact laser scanning endomicroscopy," Opt. Lett. **36**(9), 1707–1709 (2011).
8. E. R. Andresen, G. Bouwmans, S. Monneret, and H. Rigneault, "Toward endoscopes with no distal optics: video-rate scanning microscopy through a fiber bundle," Opt. Lett. **38**(5), 609–611 (2013).
9. E. R. Andresen, G. Bouwmans, S. Monneret, and H. Rigneault, "Two-photon lensless endoscope," Opt. Express **21**(18), 20713–20721 (2013).
10. Y. Kim, S. C. Warren, J. M. Stone, J. C. Knight, M. A. A. Neil, C. Paterson, C. W. Dunsby, and P. M. W. French, "Adaptive multiphoton endomicroscope incorporating a polarization-maintaining multicore optical fiber," IEEE J. Sel. Top. Quantum Electron. **22**(3), 6800708 (2016).
11. D. B. Conkey, N. Stasio, E. E. Morales-Delgado, M. Romito, C. Moser, and D. Psaltis, "Lensless two-photon imaging through a multicore fiber with coherence-gated digital phase conjugation," J. Biomed. Opt. **21**(4), 045002 (2016).

#264251 http://dx.doi.org/10.1364/OE.24.021474
Journal © 2016 Received 4 May 2016; revised 15 Jul 2016; accepted 15 Jul 2016; published 7 Sep 2016

Optics EXPRESS

12. A. M. Caravaca-Aguirre, E. Niv, D. B. Conkey, and R. Piestun, "Real-time resilient focusing through a bending multimode fiber," Opt. Express **21**(10), 12881–12887 (2013).
13. S. Farahi, D. Ziegler, I. N. Papadopoulos, D. Psaltis, and C. Moser, "Dynamic bending compensation while focusing through a multimode fiber," Opt. Express **21**(19), 22504–22514 (2013).
14. M. Plöschner, T. Tyc, and T. Čižmár, "Seeing through chaos in multimode fibers," Nat. Photonics **9**(8), 529–535 (2015).
15. J. M. Stone, F. Yu, and J. C. Knight, "Highly birefringent 98-core fiber," Opt. Lett. **39**(15), 4568–4570 (2014).
16. M. J. D. Powell, "The BOBYQA algorithm for bound constrained optimization without derivatives", *http://www.damtp.cam.ac.uk/user/na/NA_papers/NA2009_06.pdf*.
17. A. Dandridge, "Fiber optic sensors based on Mach-Zehnder and Michelson interferometers", in *Fiber optic sensors: an introduction for engineers and scientists*, E. Udd, ed. (Wiley 1991), pp. 310.
18. E. R. Andresen, S. Sivankutty, G. Bouwmans, L. Gallais, S. Monneret, and H. Rigneault, "Measurement and compensation of residual group delay in a multi-core fiber for lensless endoscopy," J. Opt. Soc. Am. B **32**(6), 1221 (2015).

1. Introduction

The development of ultra-compact optical fiber endoscopes employing spatially coherent radiation that do not require distal optical elements is a rapidly growing field. By removing the need for distal optical elements, the diameter of the endoscope is limited only by the size of the optical fiber and there is no need to develop miniaturised optical components. Such approaches can be categorised into two groups: those utilising higher order modes in a single multimode optical fiber to convey image information and those using a single optical fiber with multiple single mode cores. Both these approaches essentially determine the phase distortions of the optical fiber and then compensate them so that imaging through the optical fiber is achieved.

An early experimental demonstration for transmitting an image through a single multimode optical fiber in single pass was demonstrated in 1991 using optical phase conjugation in a photorefractive crystal [1] and from 2012 it was realised using a range of different experimental configurations [2–5]. This approach is compact, does not require specialised multicore optical fibers and is well suited to imaging fluorescence using single-photon excitation [2, 5]. Modal dispersion in multimode fiber makes it challenging to transmit the ultrashort pulses required for multiphoton excitation, although we note that progress is being made in this area by restricting the modes used to a small subset with similar optical path lengths [6].

Thompson et al. [7] demonstrated the generation of a scanning spot and lensless image formation at the distal end of a commercially available multicore optical fiber (MCF) in 2011. This approach was subsequently advanced by the demonstration of higher speed scanning spot imaging [8], and multiphoton imaging through a MCF with distal detection [9] and with a polarisation maintaining multicore optical fiber (PM-MCF) [10] in custom-designed MCFs. More recently, multiphoton imaging has been demonstrated through a commercially available MCF [11].

However, most of these approaches rely on the optical fiber being near stationary during imaging in order that the relative optical path lengths remain fixed. Choi et al. [4] demonstrated that images could be formed through single multimode fiber when the fiber tip was translated by ~0.5 mm from the position for which it was characterised, but this approach did not allow for significant deformation or bending of the fiber. Caravaca-Aguirre et al. [12] demonstrated that the combination of an FPGA control system and high speed digital micro-mirror device is capable of reforming a focused beam spot at the distal tip of a single multimode fiber following deformation in just 37 ms. However, this required measurement optics placed at the distal end of the fiber. Farahi et al. [13] used a separate single mode fiber together with a photosensitive polymer placed at the distal tip of a multimode fiber to record a hologram that produced a virtual beacon source at the distal tip of the multimode fiber. This approach enables a static focused spot to be maintained as the fiber is bent and enables the bending of the fiber at a specific point to be measured from a pre-acquired library of speckle patterns acquired for a predefined range of bend angles. However, this approach was not used to demonstrate imaging and the size of the pre-acquired library needed grows extremely rapidly as the number of bend points increases. Plöschner et al. [14] have recently shown that

Optics EXPRESS

it is possible to predict how deforming a single multimode optical fiber in a precisely defined geometry will affect the optical path lengths of the different modes, enabling scanning spot imaging through a deformed single multimode optical fiber, but the fiber in this work was static during imaging.

In this paper, we demonstrate an MCF endoscopy approach where multiphoton fluorescence imaging can be performed with all-proximal detection while the optical fiber is deformed during imaging. An initial correction procedure does require the use of distal detection optics but, once this initial correction procedure has been performed, imaging and correction for fiber deformation is achieved by proximal detection alone.

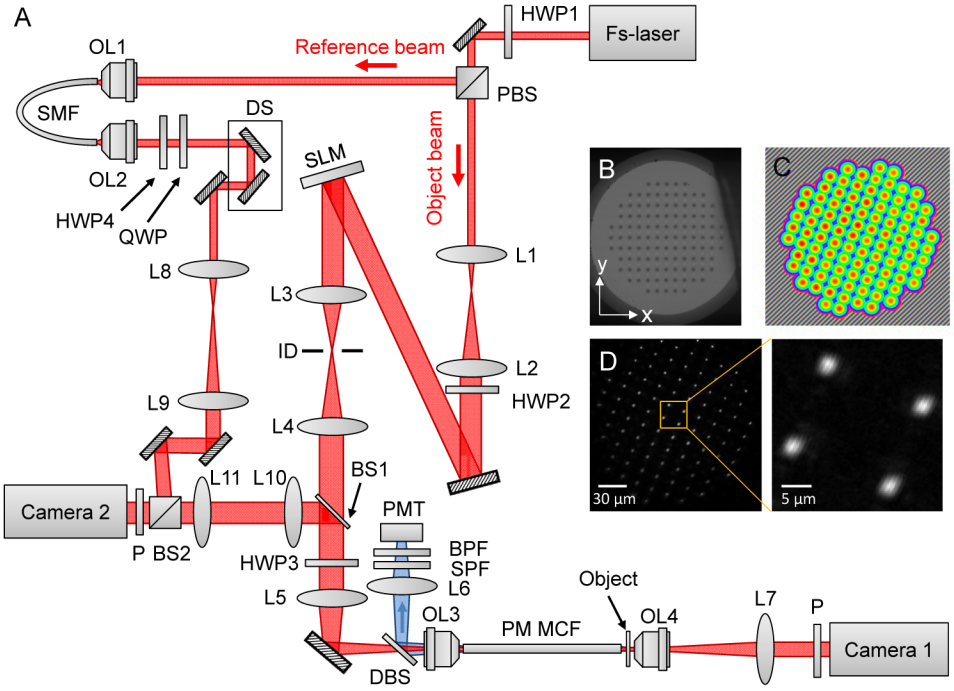

Fig. 1. (a) Experimental setup: HWP, half wave plate; PBS, polarising beam splitter; L, achromatic doublet lens; OL, microscope objective; SMF, single mode fiber; QWP, quarter wave plate; DS, delay stage; BS, non-polarising beam splitter; P, polariser; SLM spatial light modulator; ID, iris diaphragm; DBS, dichroic beam splitter; SPF, short-pass filter; BPF, band-pass filter; PMT, photomultiplier tube. (b) Optical micrograph of the PM-MCF. (c) False-color image showing a typical microlens phase profile applied to the SLM. (d) Left, exemplar interferogram acquired at Camera 2 where a background image of light from the reference beam only has been subtracted to increase the image contrast. Right, zoom in of image on left to show the interference fringes for each individual core. The scale bar in (c) and (d) indicates the scale at the proximal end of the bundle.

2. Methods

A. Double-clad polarization-maintaining multicore fiber

We used a double-clad polarization-maintaining multicore fiber (PM-MCF) with 98 cores that was designed to achieve single mode operation in each core with low cross-talk between cores at a wavelength of 800 nm. The cores are arranged in a rectangular structure with center-to-center distances of 14 µm and 16 µm in the horizontal (x) and vertical (y) directions (relative to the image shown in Fig. 1(b)). This PM-MCF has been described previously [10,15] but the details are reproduced here for completeness. Each core was manufactured from a gradient index germanium doped silica preform (Draka-Prysmian) with a pure silica jacket. The numerical aperture (NA) of the preform was 0.3 and the final core diameter in the fiber was 2

Optics EXPRESS

μm. To preserve the polarization of input light, stress-applying rods manufactured from boron doped silica (Draka-Prysmian) were inserted into the fiber – identifiable as the dark features in Fig. 1(b). The overall diameter of the MCF with 98 cores and inner cladding was 230 μm. In order to enable proximal detection of fluorescence signal, the inner cladding was jacketed with a fluorine-doped low refractive index outer cladding material (Heraeus), providing multimode guiding for fluorescence collection with a NA = 0.2. This increased the diameter of the whole double clad PM-MCF to 260 μm.

B. Experimental setup

The experimental setup was similar to that presented in our previous work [10] but with the crucial difference that the interferometer was configured to measure the relative optical path length of cores of the PM-MCF at the proximal rather than the distal end. The setup employed a Mach-Zehnder interferometer to measure the relative optical path length of each core of the PM-MCF in double pass, see Fig. 1(a). The illumination source was a modelocked Ti:Sapphire laser (Tsunami 3941-M3BB, Spectra Physics) operating at a repetition rate of 80 MHz and tuned to a centre wavelength 800 nm with a spectral bandwidth of 10.9 nm (corresponding to a coherence length of 52 μm). The beam was expanded by a factor of 2.5 (not shown in Fig. 1(a)) and then split by a polarising beam splitter cube (PBS), with one part to be delivered to the sample via the PM-MCF (length 30 cm) and the other providing a reference beam to facilitate optical path length variations between cores to be measured from interference fringes recorded by Camera 2. The relative intensity between the two beams was controlled by rotating a half-wave plate (HWP1). Light in the sample arm was expanded by a telescope (L1 and L2, focal lengths 50 and 100 mm respectively) to slightly overfill a spatial light modulator (SLM, HSPDM512, Boulder Nonlinear Systems) and its polarization was rotated by HWP2 to match the axis of the SLM. The SLM provided phase-only modulation with 512 × 512 pixels at a pitch of 15 μm.

During the process of aligning the SLM to the PM-MCF, the SLM was initially imaged onto the proximal end of the PM-MCF with a de-magnification factor of $M = 22$ by two 4-f imaging systems (L3, L4 and L5, OL3, focal lengths 200, 300 and 150 mm and magnification/NA 40 × /0.65 respectively). To focus light into the cores, a microlens array of focal length $f = 12.1$ mm was then generated on the SLM see Fig. 1(c), corresponding to a focal length of 25 μm in the object space of objective lens OL3 and giving an injection numerical aperture of approximately 0.28 at the proximal end of the fiber. The proximal end of the PM-MCF was then translated 25 μm from the focal plane of the proximal objective lens (OL3) in order to match the axial position of the focal spots generated by the SLM microlenses.

To minimize unwanted excitation light in the inner cladding of the PM-MCF, a high spatial frequency binary mask was written to areas of the SLM where zero amplitude was required. Light diffracted off-axis from these regions of the SLM was then blocked by an iris diaphragm (ID) placed between L3 and L4. A polarizer (P) placed in front of Camera 1 was used during alignment of HWP3 to ensure that light in the sample arm was correctly coupled into one axis of the PM-MCF.

Light reflected from both the proximal and distal faces of the PM-MCF was reflected by a non-polarising beam splitter (BS1, BSF10-B, Thorlabs) and imaged onto Camera 2 (sCMOS, Zyla 10-tap, Andor) through a pair of 4-f imaging systems (OL3, L5 and L10, L11, the focal lengths of L10 and L11 were 300 and 100 mm respectively) with a total magnification factor of 11.

For fluorescence imaging with distal collection, fluorescence from the object was collected by the inner cladding of the PM-MCF and reflected off a dichroic beam splitter (DBS, Di01-R594-25x36, Semrock). The proximal face of the PM-MCF was focused onto a photomultiplier tube (PMT) by lens L6. The emission was selected by a short-pass filter (SPF, E700SP, Chroma technology) and band-pass filter (BPF, HQ610/75m, Chroma technology).

For the initial measurement of the optical path length variation between the cores of the PM-MCF, the object shown in Fig. 1(a) was not present. In the reference arm, 60 cm of single

Optics EXPRESS

mode fiber (780HP, Thorlabs), i.e. twice the length of the PM-MCF, was used to match approximately the dispersion in the two arms of the interferometer. The sample and reference beams were recombined to generate interference fringes on the camera using a non-polarizing beamsplitter (BS2). Half wave plate HWP4 and quarter wave plate QWP were used to adjust the orientation of the reference beam polarization state to match that reflected from the distal end of the fiber so as to maximize the contrast of interference fringes obtained. The relative optical path length between the sample and the reference beams was adjusted to maximize the contrast of the interference fringes obtained from the distal end of the PM-MCF using the mechanical delay stage (DS). Figure 1(d) shows an exemplar image of the interferogram obtained at Camera 2. Light reflected from the proximal end of the PM-MCF does not produce interference fringes at Camera 2 as the optical path lengths of the sample and reference arms are not matched for this surface. The reference arm beam was aligned to produce a fringe pattern with a period of approximately 18 μm at the location of each fiber core on Camera 2, and the relative phases of the optical field after a double-pass of the PM-MCF could be measured. The affine transformation between the SLM pixels and the pixels of Camera 2 was calculated as described previously [7].

To correct the phase variation between the cores of the PM-MCF caused by the variation in optical pathlength of the individual cores, we used the following procedure:

1) The phase of the optical field after double-pass of the PM-MCF was calculated for each individual fiber core from the interferogram recorded on Camera 2 using the Fourier-transform method [7].

2) For each core of the fiber, the corresponding SLM microlens was identified using the affine transformation from SLM to the coordinates of Camera 2, and its phase was adjusted to remove half of the phase measured in step 1 (due to the phase difference between cores being measured in double-pass through the fiber). It is important to note that, as the optical path length of each core of the PM-MCF was measured in round trip to modulo 2π, there is a π phase ambiguity in the measured single pass optical path length.

3) A phase profile was added across the PM-MCF cores – as described in [7] – that would produce a focused beam at a distance 450 μm from the distal tip of the PM-MCF if the π phase ambiguity were not present. The position of OL4 was then adjusted to form a focused image of the focal plane on Camera 1 and an image was recorded. We note that due to the periodic distribution of cores in the PM-MCF the focus generated at the distal tip of the fiber is a periodic array of focussed spots and that this limits the maximum size of object that can be imaged using this MCF [10].

4) We then applied the following procedure to overcome the π phase ambiguity. Taking the individual cores of the PM-MCF in turn, we adjusted the appropriate microlens on the SLM to add a phase shift of π to the current core and then acquired another image on Camera 1. If the addition of the π phase shift caused the maximum pixel value in the image to increase, the π phase shift was retained, if it decreased, the phase of that core was returned to its original value. We refer to this process as the π phase-flipping optimisation.

5) Finally, in order to overcome noise in the phase measurement process, the phase corrections applied to each core were optimised to maximise the intensity of the focused spot. The phases were optimised in groups of five cores using the derivative-free non-linear optimisation algorithm BOBYQA (Bound Optimization BY Quadratic Approximation) [16]. Four iterations of this procedure were found to be sufficient to reach the maximum.

This approach makes use of the phase information obtained from the proximal interferometer measuring the double-pass optical path-length variations. An alternative

Optics EXPRESS

approach would be to employ a direct distal phase measurement scheme such as the one used in [8].

The whole process was controlled through a custom software package written in C + + . Following the optimisation above, the total average power measured at the distal end of the PM-MCF was 128 mW and the average power in the central focal spot was 0.7 mW. As reported previously [10], for the low average power in each core of the PM-MCF used here, there was no measureable increase in spectral bandwidth after propagation through the fiber cores and we therefore expect negligible pulse broadening due to self-phase modulation. We calculate the broadening due to group velocity dispersion (GVD), which is dominated by the material dispersion at 800 nm, to result in an output pulse duration of 370 fs after propagation through the 30 cm long PM-MCF. We also previously measured the optical path length variation between cores of the PM-MCF [10] and found that the standard deviation was 31.9 μm, which is less than the coherence length.

3. Results

A. Distal measurement of deformation-induced optical path length changes in PM-MCF

In order to achieve a real-time readout of deformation-induced changes in the optical path lengths of the cores of the PM-MCF, the interferogram on Camera 2 was recorded at 100 frames per second as the optical fiber was deformed by a sinusoidally oscillating loudspeaker cone operated at 1 Hz. The deformation of the fiber causes tip and tilt to be added to the phase profile at the distal tip of the PM-MCF and therefore has the effect of laterally shifting the focussed spots. Camera 1 was configured so that its acquisition was exactly synchronised to Camera 2 to provide an independent measurement of the actual shift in focal position induced by deforming the fiber.

For a frame acquired by Camera 2 at time t, the measured phase $\phi^{(i)}_{\text{measured}}(t)$ was calculated from the interferogram for every core i of the PM-MCF. We then defined a model $\phi^{(i)}_{\text{model}}$ of the phase difference at each core between t and t_{ref} to be

$$\phi^{(i)}_{\text{model}}(t) = x^{(i)} a_x(t) + y^{(i)} a_y(t) + b(t). \quad (1)$$

Here $x^{(i)}$ and $y^{(i)}$ are the x and y coordinates respectively of the i^{th} core measured at the distal tip of the PM-MCF. a_x and a_y are the tip and tilt caused by deformations of the PM-MCF and b is an overall phase change to account for small drifts over time between the reference arm and sample arm path lengths. Here we chose t_{ref} = 100 ms to allow for initial settling of the SLM (~10 ms).

Optics EXPRESS

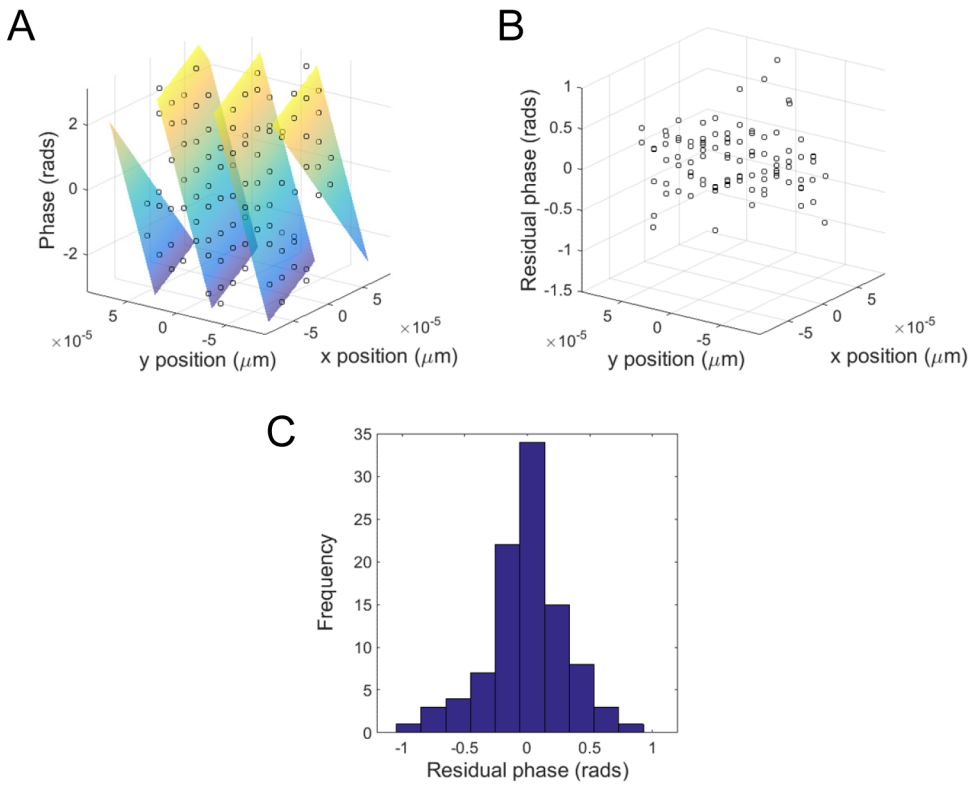

Fig. 2. Determination of tip and tilt induced by fiber deformation. (a) black circles show the calculated phase change for each fiber core between an exemplar time t and reference time t_{ref}. The phase-wrapped plane surface color-coded by phase value shows the results of the fit of the model to the data. (b) residuals of the fit to the data shown in (a). (c) histogram of the residuals shown in (b).

For each time point t, we then determined a_x and a_y by nonlinear least squares fitting of the model in Eq. (1) to the difference between the phases measured at time t and t_{ref} as described by

$$\min\left\{\sum_i \underset{-\pi..\pi}{\mathrm{mod}}\left[\left(\phi^{(i)}_{\mathrm{measured}}(t)-\phi^{(i)}_{\mathrm{measured}}(t_{\mathrm{ref}})\right)-\phi^{(i)}_{\mathrm{model}}(a_x,a_y,b)\right]^2\right\}, \quad (2)$$

where $\underset{-\pi..\pi}{\mathrm{mod}}(x)$ represents the principal value of phase for x over the range $-\pi..\pi$. The minimisation was performed using MATLAB's lsqnonlin minimisation function. An example fit is shown in Fig. 2. The randomly distributed residuals (see Figs. 2(b) and 2(c)) indicate that the model provides a good fit to the data.

The lateral shift of the focal spot position in the x and y directions p_x and p_y can then be calculated using

$$p_{x,y}=\frac{a_{x,y}}{2}\frac{\lambda}{2\pi}f, \quad (3)$$

where λ is the wavelength and f is the focal length of the distal focus. This formula accounts for the fact that the tip and tilt phase slopes are measured in round trip in the interferometer. The fitting procedure described above was then repeated for all 500 time points recorded over a 5 s acquisition period. For comparison, the position of the central focal spot was simultaneously imaged onto Camera 1, enabling the centroid position of the central spot of the

Optics EXPRESS

distal focus relative to its position at t_{ref} to be calculated. Results from both the proximal phase fitting and distal centroid estimation are plotted together in Fig. 3. We note that there are no adjustable parameters in either curve and that the two curves follow the same trajectory, illustrating the success of our proximal phase measurement method.

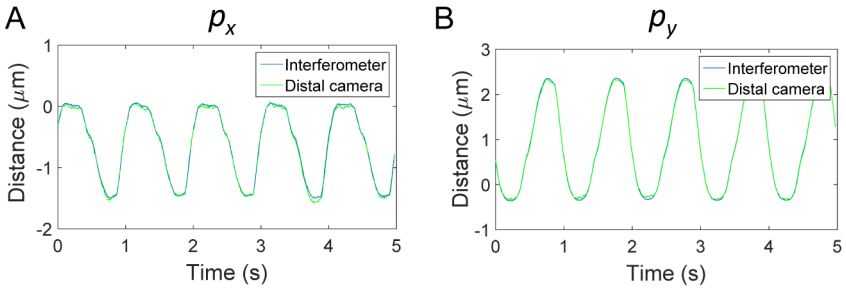

Fig. 3. Measurement of deformation-induced lateral shifts of the focus calculated from the proximal phase measurements (blue) and measured from the centroid of the distal focus spot (green). (a) and (b) show the shifts in the x and y directions respectively.

B. Multiphoton fluorescence imaging through a deforming PM-MCF

In the section above we demonstrated that we can measure the deformation-induced shift in the distal focus position proximally. We now demonstrate that, by making this measurement during an image scanning acquisition, we can use the information of the fiber deformation to correct image data obtained while the fiber is deformed by either a loudspeaker cone or by hand. Apart from the initial procedure to correct for the static phase-variations between cores, all information required to form the image is acquired at the proximal end of the PM-MCF.

Following our previous work [10], the distal focal spot position can be raster scanned over the sample by applying an appropriate phase profile to the proximal end of the PM-MCF using the SLM. However, the phase measurement procedure in the section above does not account for the additional time-varying phases applied to scan the excitation spot. It is therefore necessary to modify Eq. (2) to account for this as follows

$$\min\left\{\sum_i \underset{-\pi..\pi}{\mathrm{mod}}\left[\left(\left(\phi^{(i)}_{\mathrm{measured}}(t)-\phi^{(i)}_{\mathrm{applied}}(t)\right)-\left(\phi^{(i)}_{\mathrm{measured}}(t_{\mathrm{ref}})-\phi^{(i)}_{\mathrm{applied}}(t_{\mathrm{ref}})\right)\right)-\phi^{(i)}_{\mathrm{model}}(a_x,a_y,b)\right]^2\right\}. \quad (4)$$

Here, the phase applied to each core by the SLM to generate a focus at a specific scan position at time t is denoted by $\phi^{(i)}_{\mathrm{applied}}(t)$.

We imaged a sample consisting of two isolated 3.55 μm diameter fluorescent beads (Light Yellow, Spherotech Inc., dried onto a coverslip) using multiphoton excitation and proximal fluorescence detection through the inner cladding of the PM-MCF onto the PMT (see Fig. 1). Images were obtained while the optical fiber was deformed by the loudspeaker cone oscillating at 1 Hz (Fig. 4 top left and Visualization 1) and manually using a finger (Fig. 4 bottom left and Visualization 2).

The pixel dwell time was 30 ms, the distal focal length was 450 μm and the frame rate of Camera 2 was 416 fps. Images were formed by scanning the excitation spot over a field of view of 22 μm with 50 × 50 pixels and therefore taking 75 s. The field of view was scanned 10 times for each acquisition taking a total of 750 s. Post-acquisition, we used Eqs. (3) and 4 to calculate the lateral shift of the excitation spot caused by the deformation of the fiber and we then used this information to reassign the photons detected to the correct spatial locations, i.e. accounting for the deformation-induced lateral shift in the focal spot position.

The linear distance between the end points of the trajectory of the bend-induced perturbation of the scanning spot position relative to its desired position was 5 μm for the

Optics EXPRESS

loudspeaker and 13 μm for the manually-induced deformation. The phase change across the bundle $\Delta\phi$ can be converted to the physical change in length across the bundle ΔL using

$$\Delta\phi = \frac{2\pi}{\lambda}\xi n\,\Delta L, \tag{5}$$

where n is refractive index and ξ is the strain optic correction factor, which is typically ~0.78 in silica glass fibers [17]. This yields ΔL ~1.4 and 3.4 μm in single-pass for the loudspeaker and manual deformation respectively. This is equivalent to bending the fibre along a circular arc subtending an angle of 0.3 and 0.7° respectively, i.e. deflection ranges of 0.6 and 1.4° respectively.

The uncorrected multiphoton fluorescence image of the two beads is shown in the middle column of Fig. 4 and the corrected image is shown in the right hand column. The images demonstrate that the correction procedure has successfully accounted for the deformation-induced distortion of the fluorescence image. The offset between raw and corrected images is due to non-zero deformation-induced shift at t_{ref}. This shift could be avoided by acquiring the reference phase data when the fiber is known to be in its non-deformed state.

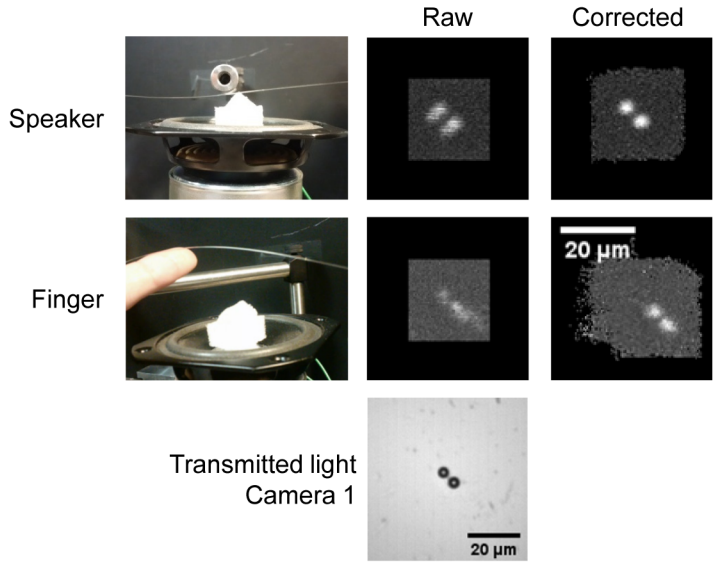

Fig. 4. Results of image correction performed for data acquired while the multicore fiber is perturbed by a loudspeaker cone (top row and Visualization 1) and by hand (middle row and Visualization 2). The left hand column shows a photo of the multicore fiber being deformed. The middle column shows the fluorescence image obtained from two fluorescent beads without correction and the right hand column shows the fluorescence image obtained with correction. All four fluorescence intensity images are shown using the same grey scale. The image on the bottom row shows a transmitted light image of the object obtained on Camera 1.

Our correction scheme requires that the fringes on Camera 2 are changing sufficiently slowly that they do not blur out during the integration time of Camera 2 (2.4 ms) and that the deformation-induced movement of the distal excitation spot during the pixel dwell time does not exceed the size of the excitation spot. In order to illustrate this, we increased the driving frequency of the loudspeaker driven deformation up to 5 Hz whilst keeping the amplitude of the drive voltage constant, see Fig. 5. This data was acquired over three full scans of the field of view each with 60 × 60 pixels (taking 324 s) but otherwise with the same parameters as above. For the configuration used here, the correction procedure works at 2 Hz and reasonably well at 3 Hz. For the 5 Hz data, the maximum deformation-induced lateral movement of the focal spot (measured by the interferometer) during a pixel dwell time is ~4 μm compared to a point spread function full-width at half maximum of ~1.8 μm measured

Optics EXPRESS

when the fiber is not deformed [10]. The measured modulation depth of the interference fringes recorded by the interferometer was not affected by the deformation of the fiber and so blurring of the fringes on Camera 2 was not the cause of the decreased image correction performance at higher loudspeaker frequencies. The performance of this system could therefore be improved in the future by recording the fluorescence signal with higher time resolution.

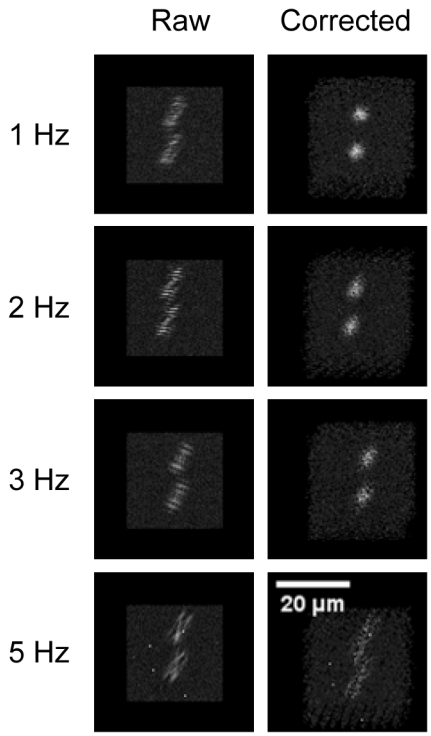

Fig. 5. Raw (left hand column) and corrected (right hand column) fluorescence images obtained with the multicore fiber perturbed by the loudspeaker cone operated at different frequencies. All images are displayed using the same grey scale.

4. Discussion

The maximum deformation-induced tip and tilt that this method could correct is limited by the requirement that the path length difference induced across the bundle (with 144 µm outer core separation in *y*-direction shown in Fig. 1(b)) does not exceed the coherence length of the source (52 µm), which would give a spot displacement range of 163 µm for the configuration used. The maximum phase change across the bundle $\Delta\phi$ permitted by this condition can be converted to the maximum physical change in length across the bundle using Eq. (5), which yields ΔL ~22 µm in single-pass. This is equivalent to bending the fibre along a circular arc subtending an angle of 9° leading to a deflection range of 18°.

It is important to note that the periodic arrangement of cores within the PM-MCF gives rise to ambiguity when measuring the tip and tilt parameters, as this causes there to be a set of periodically spaced tip and tilt parameters satisfying Eq. (2). This ambiguity effectively limits the maximum size of the object that can be imaged to 11.3 µm in the *y*-direction shown in Fig. 1(b). If the phase measurements are performed sufficiently rapidly compared to the rate of change of deformation of the fiber, then it would in principle be possible to unwrap discontinuities in measured tip and tilt to allow a larger object to be imaged. However, the periodic arrangement of cores also generates a periodic array of spots in the focal plane, as previously discussed in [10], which for the configuration used here limits the maximum size

Optics EXPRESS

of the object that can be imaged to 22.5 μm in the *y*-direction shown in Fig. 1(b). In order to increase the size of object that can be imaged, it is necessary to decrease the spacing of the fiber cores or to arrange them in a less ordered way [7, 11]. Correction of perturbations larger than those discussed in the paragraph above would require that either the coherence length of the source is increased or that an adaptive approach such as the one described in [18] is applied to correct for group-delay dispersion as the fiber is deformed.

The calculation required for the phase-fitting approach was implemented in the high-level programming environment MATLAB using its standard in-built nonlinear least squares minimisation function. It was therefore not possible to implement the phase fitting procedure and image correction in real time. Given better optimized software we expect that this calculation and the subsequent image correction could be applied in real time using a modern desktop computer.

In our current system, the two ends of the fiber are maintained in a fixed position while the fiber in between is dynamically deformed. Because the positions of the two ends are fixed, deformation of the fiber introduces tip and tilt to the wavefront at the distal end of the fiber causing lateral translation of the excitation spot. In the future, it might be possible to use our approach to measure and then correct for rotation of one end of the PM-MCF relative to the other by including a radial quadratic phase parameter to the fitting model used. Higher order distortion modes could also potentially be determined, but this will depend on the signal to noise ratio achieved by the interferometric measurement of the phase for each core. Ultimately, the theoretical limit on the number of distortion modes that could be determined is given by the number of fiber cores in the bundle.

5. Conclusions

We have demonstrated a multiphoton lensless endoscope system capable of forming an image during dynamic deformation of the imaging fiber. An initial calibration procedure requires the use of optics placed at the distal end of the fiber in order to determine and then correct for the optical path-length differences between cores of the PM-MCF but, following this step, all detection is performed proximally. Our approach measures the optical path-length difference between cores of a PM-MCF in round trip using a Mach-Zehnder interferometer with the interferogram recorded in a single camera frame at the proximal end of the fiber. We apply a fitting procedure to the optical phase measured for each core in order to determine the fiber deformation-induced tip and tilt of the wave front at the distal end. Knowledge of the deformation-induced tip and tilt allows us to correct for the deformation-induced translation of the focal spot at the distal tip of the fiber in post-processing that otherwise would distort and blur the image. We demonstrated that this approach is successful for deformations of the fiber induced by a moving loudspeaker cone and by hand. Our image acquisition procedure currently uses the SLM to perform image scanning and is relatively slow (30 ms pixel dwell time). In the future, it will be possible to introduce rapid galvo mirror beam scanning, as has already been demonstrated for imaging in transmission through a static fiber [8]. Our results show that the ability of our system to correct for dynamic fiber deformation is limited by the temporal resolution for the fluorescence photodectection (30 ms – equal to the pixel dwell time). In the future, this could easily be improved by e.g. time-tagging photodectections with higher temporal precision.

Funding

This work was funded by a UK Engineering and Physical Sciences Research Council (EPSRC) Healthcare Technologies Challenges for Engineering research grant (EP/K020102/1).

Acknowledgments

The authors would like to thank Dr. B. Sherlock for helpful discussions.